UC Berkeley
UC Berkeley Previously Published Works

Title
Effects of Fe electrolyte impurities on Ni(OH)2/NiOOH structure and oxygen evolution activity

Permalink
https://escholarship.org/uc/item/1zp2p74w

Journal
Journal of Physical Chemistry C, 119(13)

ISSN
1932-7447

Authors
Klaus, S
Cai, Y
Louie, MW
et al.

Publication Date
2015-04-02

DOI
10.1021/acs.jpcc.5b00105

Peer reviewed

eScholarship.org Powered by the California Digital Library
University of California

THE JOURNAL OF PHYSICAL CHEMISTRY C

Article

pubs.acs.org/JPCC

Effects of Fe Electrolyte Impurities on $Ni(OH)_2$/NiOOH Structure and Oxygen Evolution Activity

Shannon Klaus, Yun Cai, Mary W. Louie, Lena Trotochaud, and Alexis T. Bell*

Joint Center for Artificial Photosynthesis, Materials Science Division, Lawrence Berkeley National Laboratory, Berkeley, California 94720, United States and

Department of Chemical and Biomolecular Engineering, University of California, Berkeley, California 94720, United States

Supporting Information

ABSTRACT: Ni-(oxy)hydroxide-based materials are promising earth-abundant catalysts for electrochemical water oxidation in basic media. Recent findings demonstrate that incorporation of trace Fe impurities from commonly used KOH electrolytes significantly improves oxygen evolution reaction (OER) activity over NiOOH electrocatalysts. Because nearly all previous studies detailing structural differences between α-$Ni(OH)_2$/γ-NiOOH and β-$Ni(OH)_2$/β-NiOOH were completed in unpurified electrolytes, it is unclear whether these structural changes are unique to the aging phase transition in the Ni-(oxy)hydroxide matrix or if they arise fully or in part from inadvertent Fe incorporation. Here, we report an investigation of the effects of Fe incorporation on structure–activity relationships in Ni-(oxy)hydroxide. Electrochemical, in situ Raman, X-ray photoelectron spectroscopy, and electrochemical quartz crystal microbalance measurements were employed to investigate $Ni(OH)_2$ thin films aged in Fe-free and unpurified (reagent-grade) 1 M KOH (<1 ppm Fe). We find that Ni films aged in unpurified electrolyte can incorporate ≥20% Fe after 5 weeks of aging, and the maximum catalyst activity is comparable to that reported for optimized $Ni_{1-x}Fe_xOOH$ catalysts. Conversely, Fe-free $Ni(OH)_2$ films exhibit a substantially lower activity and higher Tafel slope for the OER. Films aged in Fe-free electrolyte are predominantly disordered β-$Ni(OH)_2$/β-NiOOH if maintained below 0.7 V vs Hg/HgO in 1 M KOH and will "overcharge" to form a mixture of γ- and β-NiOOH above this potential. Fe-containing $Ni(OH)_2$ films evidence a lesser extent of β-$Ni(OH)_2$ formation and instead exhibit NiOOH structural changes in accordance with the formation of a NiFe-layered double hydroxide phase. Furthermore, turnover frequency calculations indicate that Fe is the active site within this phase, and above ~11% Fe content, a separate, Fe-rich phase forms. These findings are the first to demonstrate the in situ changes in the catalyst structure resulting from the incorporation of Fe electrolyte impurities within Ni-(oxy)hydroxide, providing direct evidence that a Ni–Fe layered double (oxy)hydroxide (LDH) phase is critical for high OER activity.

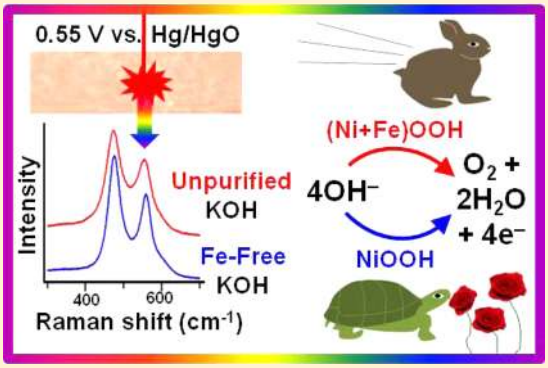

1. INTRODUCTION

Electrochemical water-splitting to form molecular oxygen (O_2) and hydrogen (H_2) offers a promising means for the storage of energy generated from intermittent energy sources, such as wind and solar.[1,2] A major challenge to accomplish this conversion efficiently, however, is the slow kinetics of the oxygen evolution reaction (OER, $4OH^- \rightarrow 2H_2O + O_2 + 4e^-$ in base and $2H_2O \rightarrow 4H^+ + O_2 + 4e^-$ in acid) at the anode, which results in a large reaction overpotential.[1−3] To improve the overall energy efficiency of such systems, a highly active and cost-effective electrocatalyst for the OER is critical.

In alkaline electrolyte, nickel-based materials are particularly promising OER catalysts because of their high stability and earth abundance.[4,5] The OER-active phase of nickel catalysts has been shown to be Ni^{3+} or a mixture of Ni^{3+} and Ni^{4+} present as a NiOOH-type structure.[6−9] At potentials well below the onset of the OER, the catalyst is present as $Ni(OH)_2$, and prior to the onset of oxygen evolution, this phase is oxidized to NiOOH via the reaction $Ni(OH)_2 + OH^- \rightarrow NiOOH + H_2O + e^-$.[5,8] Numerous studies have reported that the activity of NiOOH can be increased in two ways: (1) by addition of Fe to NiOOH[10−21] and (2) by transformation of the OER active phase γ-NiOOH to β-NiOOH via aging as shown in the Bode scheme in Figure 1.[5,22−28]

Given that addition of Fe is a primary means to improve the activity of NiOOH catalysts, previous work from our group has focused on elucidation of the effects of Fe within the $Ni(OH)_2$/NiOOH structures. X-ray absorption spectroscopy (XAS) investigations show that although no change occurs in the Ni–O bond length with Fe addition, the Fe–O bond length exhibits a significant contraction upon electrochemical oxidation to $Ni_{1-x}Fe_xOOH$.[29] Corresponding density-func-

Received: January 5, 2015
Revised: February 27, 2015
Published: March 3, 2015

ACS Publications © 2015 American Chemical Society

DOI: 10.1021/acs.jpcc.5b00105
J. Phys. Chem. C 2015, 119, 7243−7254

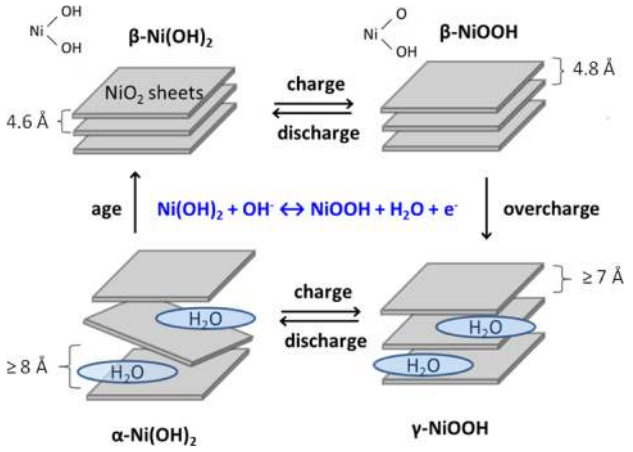

Figure 1. Bode scheme[28] for the $Ni(OH)_2$/NiOOH redox transformation.

tional theory calculations show that this Fe−O bond contraction optimizes the binding energies of OER reaction intermediates over these sites, which is the proposed mechanism of improved OER activity over $Ni_{1-x}Fe_xOOH$ materials.

Trotochaud et al.[30] recently revealed that the increase in OER activity observed with aging in KOH is not due to the transition of γ-NiOOH to β-NiOOH, as had been concluded in previous studies. They show that Fe-free NiOOH is a poor catalyst for the OER, exhibiting an overpotential in excess of 500 mV at 10 mA cm^{-2}. Instead, increased activity with aging arises from Fe impurities present in KOH electrolyte, which readily incorporate into the NiOOH films. This work also showed that 25% *codeposited* Fe produces a Ni−Fe layered double hydroxide, which inhibits the aging phase transformation of α-$Ni(OH)_2$ to β-$Ni(OH)_2$. However, the effects of *Fe-impurity* incorporation on structural changes were not addressed.

Because nearly all previous efforts aimed at investigating structural differences between α-$Ni(OH)_2$/γ-NiOOH and β-$Ni(OH)_2$/β-NiOOH were likely carried out using Fe-contaminated KOH, it is not clear to what degree these structural changes are due to unintentional Fe incorporation and how structural changes affect activity in the absence of Fe.[24,25] In this study, we attempt to separate the effects of Fe-incorporation and aging on NiOOH structure by employing electrochemistry, spectroscopy, and microgravimetry techniques to investigate $Ni(OH)_2$/NiOOH films aged in both Fe-free and unpurified KOH electrolyte. These findings distinguish the true effects of aging vs Fe-incorporation on thin film Ni-(oxy)hydroxide OER catalyst structure and activity, specifically that (1) in Fe-free electrolyte, the traditional description of structural changes developed by Bode holds, despite previous aging/overcharging studies completed in the presence of Fe contaminants, (2) Fe incorporates into the Ni-(oxy)hydroxide lattice and forms a distinct structure that is consistent with an NiFe-layered double (oxy)hydroxide (LDH) structure, and (3) it is the Fe-sites within this mixed Ni−Fe LDH phase that are critical for the improved OER activity observed in unpurified KOH.

2. EXPERIMENTAL SECTION

2.1. Electrocatalyst Deposition and Aging. Experiments were conducted in both purified (Fe-free) and unpurified reagent-grade (containing Fe impurities) 1 M KOH electrolyte. Fe-free 1 M KOH was prepared from 45% Baker Analyzed Electronic grade KOH solution (VWR JT3144-3) and purified according to the method outlined by Trotochaud et al. (see Supporting Information Section S1).[30] Unpurified 1 M KOH solutions were prepared using ACS reagent-grade KOH pellets (≥85%, ≤0.001% Fe, Sigma-Aldrich 221473). In addition, all experiments were performed in a PFA beaker to avoid possible contamination due to glass-etching.[10]

$Ni(OH)_2$ films were deposited electrochemically onto 5 mm diameter Au electrodes. Prior to each deposition, a Au electrode was polished mechanically with 1 and 0.05 μm diameter alumina, with sonication in H_2O (18 MΩ cm resistance, Milli Q Millipore) for 10 min between each polishing step. The Au electrode was then cycled electrochemically from −1.0 to 0.7 V vs a Hg/HgO reference electrode filled with 1 M KOH (CH Instruments) at 10 mV s^{-1} in Fe-free 1 M KOH until the cyclic voltammogram was fully stabilized (typically ∼50 cycles). This procedure ensured that Ni deposition occurred on a fully stabilized electrode surface. Alternatively, for Raman experiments, the Au electrode was roughened electrochemically in 0.1 M KCl (Sigma-Aldrich P3911) through application of a previously reported waveform (see Supporting Information S2).[31] $Ni(OH)_2$ was electrodeposited from a nitrogen-sparged, high-purity 0.01 M $Ni(NO_3)_2$ solution (from 99.999% nickel nitrate hexahydrate, Sigma-Aldrich 203874) using a cathodic geometric-surface-area current density of 1 mA cm^{-2}. The deposition time was 75 s over quartz crystal microbalance (QCM) and rotating disc electrodes (RDEs) to obtain films with ∼30 nm thickness based on a QCM mass-change deposition profile (Supporting Information S3). Films deposited for Raman experiments are estimated to be ∼12−15 nm thick because of the roughness of the underlying Au substrate.

A coiled Pt wire served as the counter electrode for all experiments, with a separate Pt wire used for Ni deposition. Both Pt wire counter electrodes were periodically cleaned by overnight soaking in 5 M nitric acid or 1 M sulfuric acid.

Aging of $Ni(OH)_2$ films was carried out by immersing the $Ni(OH)_2$/Au electrode in 1.125 mL of Fe-free or unpurified 1 M KOH at room temperature and in the absence of applied electrochemical potential. For each day of electrochemical measurements, fresh KOH electrolyte solution was used. To investigate the progressive aging process, the OER performance was measured each day on the same $Ni(OH)_2$/Au electrode for a period of 6 days.

2.2. Electrochemical Measurements. All rotating disk electrode (RDE) experiments were performed on 5 mm Au electrodes (Pine Research Instrumentation). A coiled Pt wire served as the counter electrode, and all potentials are recorded vs a Hg/HgO reference electrode. The potential of the Hg/HgO reference was routinely checked against another Hg/HgO reference electrode to ensure electrode stability and differed by 2.5 mV or less. Current−voltage curves for $Ni(OH)_2$ films were acquired with RDEs immersed in 45−50 mL of freshly prepared Fe-free or unpurified 1 M KOH solution using a rotation rate of 1600 rpm and a sweep rate of 10 mV s^{-1}. The typical potential range for OER measurement vs Hg/HgO was 0.00−0.65 V (for regular KOH) and 0.00−0.92 V (for Fe-free KOH), and the 12th voltammogram cycle is reported. All electrochemical potentials reported here were corrected for uncompensated series resistance (R_u), which was determined by potentiostatic electrochemical impedance spectroscopy

DOI: 10.1021/acs.jpcc.5b00105
J. Phys. Chem. C 2015, 119, 7243−7254

(PEIS). Generally, R_u was ∼4−6 Ω in 1 M KOH solution. Unless otherwise mentioned, all potentials cited in this work are referenced to the Hg/HgO electrode. The overpotential, η, was calculated using the equation $\eta = E_{meas}$ (internally corrected for 95% R_u) − E_{rev}, where E_{meas} is the potential measured vs Hg/HgO and E_{rev} is the reversible potential of the OER vs Hg/HgO (0.306 V at pH 14 or 0.365 V at pH 13). All reported current densities were calculated on the basis of geometric surface area.

2.3. Characterization. The Ni and Fe content of films aged in regular KOH were measured by inductively coupled plasma optical emission spectrometry (ICP-OES, Optima 7000 DV, PerkinElmer). Films were dissolved overnight in 5 M nitric acid (Sigma-Aldrich 84385) and sonicated for 1 min prior to dilution. Final solutions contained 5 wt % nitric acid, and concentrations were calculated using an internal yttrium standard (Sigma-Aldrich 01357) and 0−500 ppb Ni and Fe calibration standards (Sigma-Aldrich 28944 and 43149, respectively).

X-ray photoelectron spectroscopy (XPS) studies were carried out using a Kratos Axis Ultra spectrometer with a Mg Kα nonmonochromated flood source (10 mA, 15 kV, spectra acquired with a 20 eV pass energy, 50 meV step energy, and a dwell time of 200 ms) to avoid the Ni Auger features in the Fe 2p region present with the Al source. The base chamber pressure was 10^{-9} Torr, and no charge neutralization was applied. CasaXPS (Casa Software, Ltd.) was used for sample analysis. Baseline and nonmonochromated satellite subtractions were applied (see examples in Supporting Information Figure S4.1), and all binding energies were adjusted to the adventitious carbon C 1s signal at 284.8 eV to compensate for charging effects.

Electrochemical quartz crystal microbalance (QCM) measurements were carried out with a Stanford Research Systems QCM 200. The Au/Ti quartz crystal was stabilized in 1 M KOH prior to electrodeposition, and the deposition current was adjusted for the larger area of this electrode (approximately 1.38 cm^2). Film mass changes were estimated from changes in the resonance frequency using the Sauerbrey equation, $\Delta f = -C_f \Delta m$, where Δf is the observed frequency change (Hz), C_f is the sensitivity factor of the quartz crystal, and Δm is the change in mass per unit area ($\mu g\ cm^{-2}$).[32] The quartz crystal sensitivity factor, 54.5 ± 0.5 Hz μg^{-1} cm^2, was calibrated by faradic deposition of Ag metal from a 0.05 M silver nitrate solution and is an average of three measurements. (Further information regarding QCM calibration in Supporting Information S3.)

An epoxy-free version of our previously described Teflon cell[24,25,33] was built in-house and used for the combined electrochemical and in situ Raman spectroscopy studies. A $Ni(OH)_2$ film deposited over a 5 mm electrochemically roughened Au disc sheathed in Teflon served as the working electrode. All Raman experiments were completed in 0.1 M KOH as a result of considerable background signal in 1 M KOH. In situ Raman spectra of the electrodes were recorded using a confocal Raman microscope (LabRam HR, Horiba Jobin Yvon). A high numerical aperture water-immersion objective (70× magnification, N.A. = 1.23, LOMO) was used to achieve a high collection efficiency. Prior to each experiment, the objective was wrapped in 0.001 in. PFA film (McMaster Carr) to avoid corrosion, and a droplet of water was placed between the objective and film to preserve the refractive index.[24,25,33]

Raman spectra were acquired with 1−2 mW of power (measured at the sample surface) delivered by a laser operating at 633 nm, with a laser spot size of ∼1 μm. Each Raman spectrum was recorded with a resolution of 1 cm^{-1} by averaging three scans, each of 3 s duration. For these experiments, the electrode potential was scanned at a rate of 1 mV s^{-1}. The spectral position was checked against a Si wafer prior to each sample scan and recalibrated if >1 cm^{-1} variation of the 520.7 cm^{-1} silicon phonon mode was observed. To more clearly show the Raman peaks within this region, high-wavenumber (3000−3800 cm^{-1}) spectra were background-subtracted within the Raman instrument software (Labspec).

3. RESULTS

3.1. Electrochemical Characterization of Aged $Ni(OH)_2$ Films by Cyclic Voltammetry. Extended electrode immersion in alkaline electrolyte converts the as-deposited α-$Ni(OH)_2$ phase to the more compact β-$Ni(OH)_2$ structure in a process referred to as aging.[4,5,25,27,28,34] To track electrochemical changes with electrode aging, cyclic voltammograms (CVs) were obtained for $Ni(OH)_2$ films freshly prepared and after each day of aging in 1 M Fe-free (Figure 2a) and unpurified (Figure 2b) KOH. Figure 2a shows that the OER current decreases when $Ni(OH)_2$ is aged in Fe-free electrolyte, whereas a dramatic increase in the OER current occurs for $Ni(OH)_2$/NiOOH cycled in unpurified electrolyte, even on day 0 after just 12 voltammogram cycles.

With initial cycling, a significant oxidation wave is observed at 0.43 V vs Hg/HgO for samples in both purified and unpurified electrolyte. This feature is attributed to the oxidation of Ni in the film.[5,8] The position of the oxidation wave maximum shifts to 0.47 V after 6 days of aging in Fe-free KOH and to 0.50 V after 6 days of aging in unpurified KOH.

The voltammograms recorded in Fe-free electrolyte during days 1−3 clearly display two peaks within the Ni(II)/Ni(III) oxidation region. Two smaller oxidation features, which are similar to those reported by Trotochaud et al.,[30] are also observed after the primary oxidation wave. The first feature, centered at 0.6 V, diminishes with aging, whereas the second feature emerges on day 1 at ∼0.7 V and intensifies with aging in the absence of impurities. Note that when Fe impurities are present, these two smaller oxidation waves at higher potentials would be obscured by significant oxygen evolution current.

3.2. Fe Impurity Uptake and Effects on OER Activity. The composition of $Ni(OH)_2$ films aged in 1 M KOH was determined using surface (XPS) and bulk (ICP-OES) techniques (Figure 3). No evidence for the accumulation of Fe was observed for Ni films aged in Fe-free electrolyte from XPS (Supporting Information S4). KOH solutions (1 M) made from ACS reagent-grade KOH pellets (≤0.001% Fe) are estimated to contain ≤0.66 ppm Fe. Using this unpurified electrolyte, the Ni film (∼30 nm thick) consists of ∼5% Fe after just 12 voltammogram cycles. The Fe content increases to 23−26% of total metal in the film after extended aging (38 days). The peak potentials of the $Ni(OH)_2$/NiOOH redox waves continue to shift toward more oxidizing potentials with each subsequent day of aging (Supporting Information S5), evidence that Fe still continues to incorporate, even after more than 1 month of aging.

The Fe content of the film appears to increase logarithmically with respect to aging time, and Fe contents determined from both XPS and ICP-OES are similar. Elemental analysis also shows that, in general, total film mass is comparable between

DOI: 10.1021/acs.jpcc.5b00105
J. Phys. Chem. C 2015, 119, 7243−7254

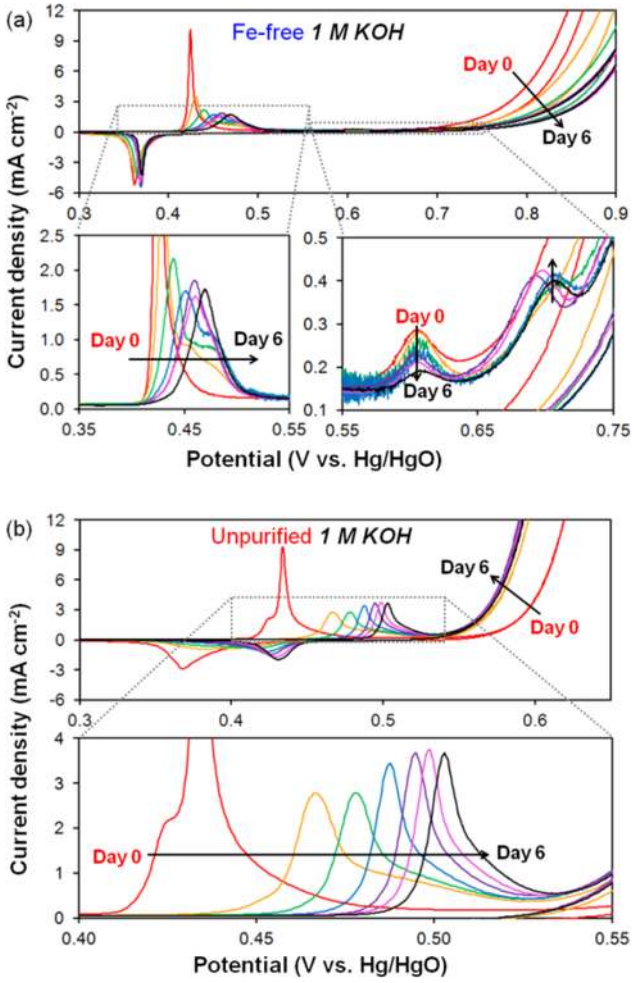

Figure 2. Cyclic voltammograms obtained for $Ni(OH)_2$ films deposited on polished Au RDEs. Voltammograms were collected at 10 mV s^{-1} and 1600 rpm in a (a) Fe-free and (b) unpurified 1 M KOH after each day of aging in either Fe-free or unpurified 1 M KOH, respectively. The oxygen evolution equilibrium potential is 0.306 V vs Hg/HgO in 1 M KOH.

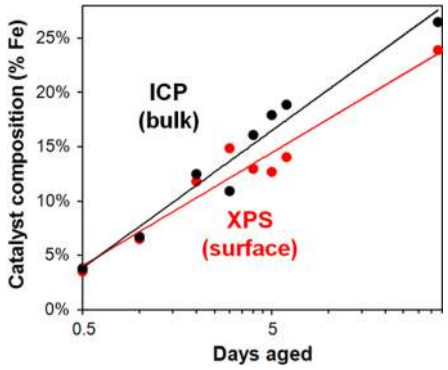

Figure 3. Iron content of $Ni(OH)_2$ films deposited on polished Au-RDEs measured from X-ray photoelectron spectroscopy (XPS) and inductively coupled plasma optical emission spectroscopy (ICP-OES) vs days aged in unpurified 1 M KOH. Lines show a logarithmic best-fit ($y = a \ln(x) + b$) to each data set. Values of a and b for each data set can be found in the Supporting Information file.

samples, indicating the films are not dissolving in the aging solution. This is consistent with known values for $Ni(OH)_2$ solubility (see explanation and table in SI S6).[35]

Ni films aged in unpurified 1 M KOH exhibit a much lower overpotential at 10 mA cm^{-2} than films aged in Fe-free electrolyte (Figure 4). Activities were comparable between 0.1

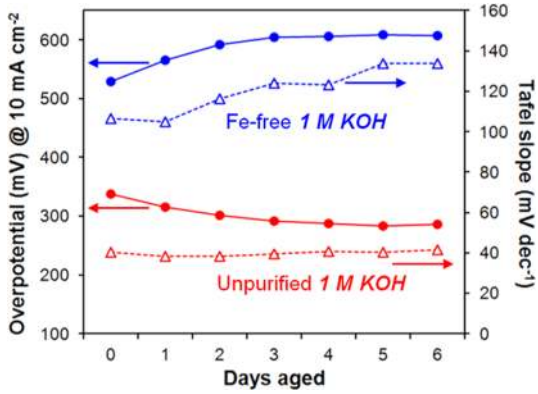

Figure 4. Effect of aging on the overpotential at 10 mA cm^{-2} geometric current density (filled circles) and Tafel slope (open triangles) for $Ni(OH)_2$ films deposited on polished Au-RDEs aged in Fe-free (blue) vs unpurified (red) 1 M KOH.

and 1 M KOH (Supporting Information S7). The overpotential for Fe-free films at 10 mA cm^{-2} is 529 mV and increases with aging, stabilizing at ~605 mV after 3 days. The overpotential for films aged in unpurified electrolyte is minimized at 280 mV after 5 days, then slightly increases by ~7 mV with subsequent aging. This overpotential is comparable to those obtained with intentional Fe incorporation.[10,24]

The OER Tafel slope for Fe-free films (Figure 4, Tafel plots in Supporting Information S8), was 106 mV dec^{-1} on day 0 and increased to 134 mV dec^{-1} by day 6; both of these values are significantly higher than the Tafel slopes previously reported for both freshly prepared and aged Ni electrocatalysts in which Fe impurities were presumably present.[9,23,36,37] In contrast, $Ni(OH)_2$ films cycled and aged in unpurified 1 M KOH exhibited an initial Tafel slope of 45−55 mV dec^{-1}, which decreased to ~40 mV dec^{-1} within 12 voltammogram cycles. The Tafel slope remained stable at 38−40 mV dec^{-1} through 6 days of aging; this value is consistent with previous Tafel slopes recorded over Ni−Fe (oxy)hydroxide electrocatalysts.[12,16,17,24]

All current densities presented are calculated on the basis of geometric electrode surface areas. A plot of current density (j at η = 300 mV) and overpotential (η at j = 10 mA cm^{-2}) as a function of surface composition is shown in Figure 5. Maximum OER activity, with j = 25−28.7 mA cm^{-2} and η = 280 mV is reached with 12−17% Fe incorporation. Compared with the activities for Fe-free NiOOH, these changes represent a 200-fold increase in current density and a nearly 250 mV decrease in overpotential. With further incorporation of Fe, no additional activity enhancement is observed.

3.3. In Situ Raman Spectroscopy of Aged $Ni(OH)_2$ Thin Films. The effects of aging on the composition and structure of $Ni(OH)_2$ films were followed by in situ Raman spectroscopy. Spectra of $Ni(OH)_2$/NiOOH films, obtained before and after 6 days of aging in Fe-free and unpurified 1 M KOH, were acquired in 0.1 M KOH during 1 mV s^{-1} oxidation sweeps and are presented in Figure 6.

For the films aged in Fe-free KOH, Raman peaks are observed on day 0 (Figure 6a) at 453 and 495 cm^{-1} for potentials between 0.0 and 0.4 V. These features then rapidly attenuate with increasing potential. Starting at 0.4 V, peaks

DOI: 10.1021/acs.jpcc.5b00105
J. Phys. Chem. C 2015, 119, 7243−7254

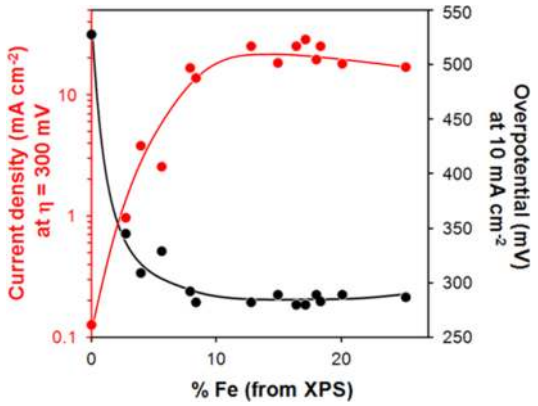

Figure 5. Oxygen evolution activity of electrodeposited NiOOH films deposited on Au RDEs at 300 mV overpotential and 10 mA cm^{-2} geometric current density in 1 M KOH as a function of Fe content. Curves are included to guide the eye.

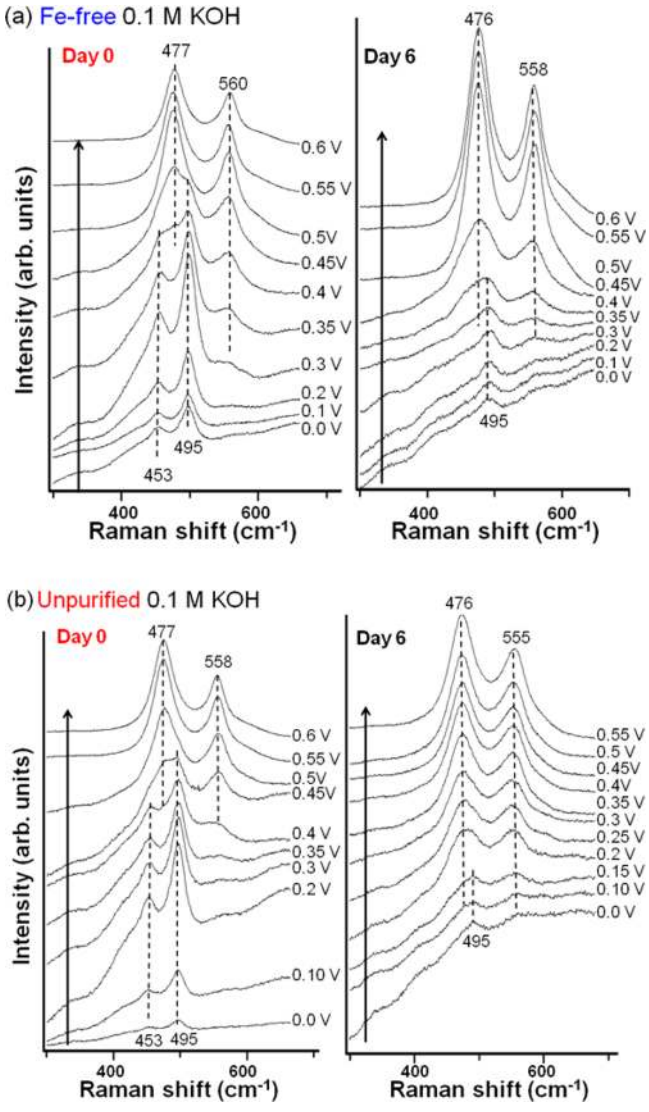

Figure 6. In situ Raman spectra collected over Ni(OH)$_2$/NiOOH films deposited on roughened Au in (a) Fe-free and (b) unpurified 0.1 M KOH on Day 0 and Day 6. Potentials are reported vs Hg/HgO. The oxygen evolution equilibrium potential is 0.365 V vs Hg/HgO in 0.1 M KOH.

emerge at 477 and 560 cm^{-1}; these features intensify as the potential is increased to 0.6 V (i.e., through the oxidation wave observed in CVs). After 6 days of aging in Fe-free KOH, only a weak feature at 495 cm^{-1} is observed at 0 V, and the 480/560 cm^{-1} peaks first appear at 0.35 V.

When films are aged in unpurified KOH (Figure 6b), the Raman bands observed initially on day 0 at 453 and 495 cm^{-1} diminish with increasing applied potential, whereas the 477 and 558 cm^{-1} Raman peaks are observed for potentials above 0.4 V. On day 6, the band at 495 cm^{-1} is also present at 0 V but is obscured by the Raman signals at 476 and 555 cm^{-1} for potentials of 0.2 V and above.

Raman spectra were also acquired at high wavenumbers (3000−3800 cm^{-1}) to observe the ν(O−H) modes of the Ni(OH)$_2$ phases (Figure 7).[8] In Fe-free electrolyte at 0.2 V, a

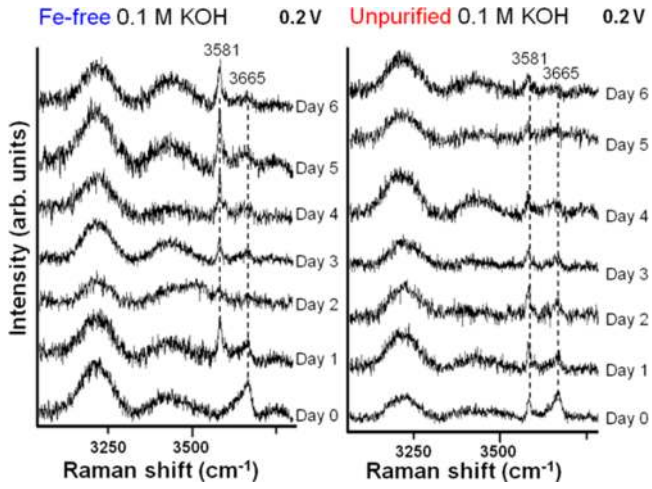

Figure 7. In situ Raman spectra collected over Ni(OH)$_2$ films deposited on roughened Au and recorded at 0.2 V vs Hg/HgO in Fe-free and unpurified 0.1 M KOH. The oxygen evolution equilibrium potential is 0.365 V vs Hg/HgO in 0.1 M KOH.

3665 cm^{-1} Raman band predominates at day 0, whereas a feature at 3581 cm^{-1} appears after a day of aging. With continued aging, the band at 3665 cm^{-1} decreases in intensity, and that at 3581 cm^{-1} becomes stronger. In unpurified electrolyte, the bands at 3581 and 3665 cm^{-1} are both present on day 0, and the intensity of both peaks decreases with aging. By day 6, there is minimal evidence for the band at 3665 cm^{-1}, and only a small feature at 3581 cm^{-1} is observed. (Additional Raman spectra are available in Supporting Information S9.)

3.4. Electrochemical Quartz Crystal Microgravimetry.

Electrochemical quartz crystal microbalance experiments were completed to track the conversion of α-Ni(OH)$_2$ to β-Ni(OH)$_2$ with aging in Fe-free and unpurified KOH. Electrochemical microgravimetry has previously been used to differentiate the α/γ and β/β phase couples: an increase in film mass occurs during the oxidation of α-Ni(OH)$_2$ to γ-NiOOH as a result of intercalation of water and ions, whereas film mass decreases or remains constant during the oxidation of β-Ni(OH)$_2$ to β-NiOOH.[27,38] For Ni(OH)$_2$ films initially cycled in both Fe-free and unpurified 0.1 M KOH, there is a 10 Hz decrease in frequency (SI S10), corresponding to a ∼160 ng cm^{-2} increase in mass during Ni(OH)$_2$ oxidation to NiOOH (Figure 8). By contrast, samples aged 6 days in either purified or unpurified KOH exhibit a decrease in mass upon oxidation. However, after 6 days of aging, the ∼110 ng cm^{-2} mass density decrease

DOI: 10.1021/acs.jpcc.5b00105
J. Phys. Chem. C 2015, 119, 7243−7254

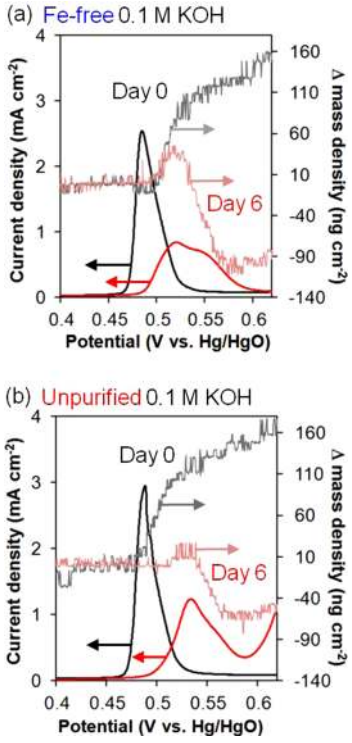

Figure 8. QCM mass density change with concurrent 10 mV s^{-1} potential scans for $Ni(OH)_2$ films deposited on Au/Ti quartz crystals in (a) Fe-free and (b) unpurified 0.1 M KOH before and after 6 days of aging in 1 M KOH. The oxygen evolution equilibrium potential is 0.365 V vs Hg/HgO in 0.1 M KOH.

observed during film oxidation for the Fe-free films is much greater than the ~50 ng cm^{-2} decrease for films aged in unpurified KOH.

3.5. Electrochemical Overcharging of the $Ni(OH)_2$/NiOOH Structure. It was previously reported that β-NiOOH can transform to γ-NiOOH via "overcharging" at potentials exceeding 0.7 V;[27,28] this conversion was investigated by maintaining films below this threshold during 6 days of aging and then applying a potential scan to 0.85 V. The results of this overcharging cycle for a roughened Au electrode are shown in Figure 9 (corresponding cycles over a QCM are presented in SI 11). As expected, the main oxidation feature of the overcharge cycle (red) aligns with that of the last stabilization cycle to 0.7 V (black). However, as the potential is increased to 0.85 V, a large oxidation feature is observed at 0.79 V. Subsequent CV cycles (purple) show a cathodic shift of the primary Ni oxidation wave (from 0.53 to 0.50 V) and the presence of a shoulder at ~0.52 V. An additional oxidation feature emerges at ~0.66 V, and the 0.79 V oxidation peak present in the first overcharge cycle is diminished and shifted cathodically to ~0.76 V.

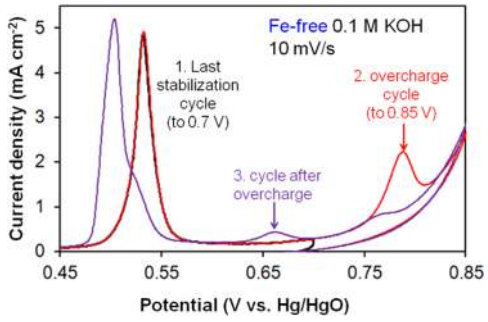

Figure 9. Cyclic voltammogram of an aged $Ni(OH)_2$ film in 0.1 M Fe-free KOH (after 6 days of aging in 1 M Fe-free KOH) with a 10 mV s^{-1} scan rate. The electrodes were stabilized to 0.7 V before a 10 mV s^{-1} overcharge scan to 0.85 V. The oxygen evolution equilibrium potential is 0.365 V vs Hg/HgO in 0.1 M KOH.

Corresponding QCM measurements, shown in Figure 10, were completed to track mass changes before and after the 0.85 V overcharging scans in both Fe-free and unpurified KOH. For the Ni film aged in Fe-free electrolyte, a decrease in mass is observed with the primary oxidation wave from 0.54 to 0.58 V. After overcharge, the primary oxidation wave more closely resembles that of the day 0 electrode (Figure 8), and essentially no mass change is observed during the primary oxidation wave.

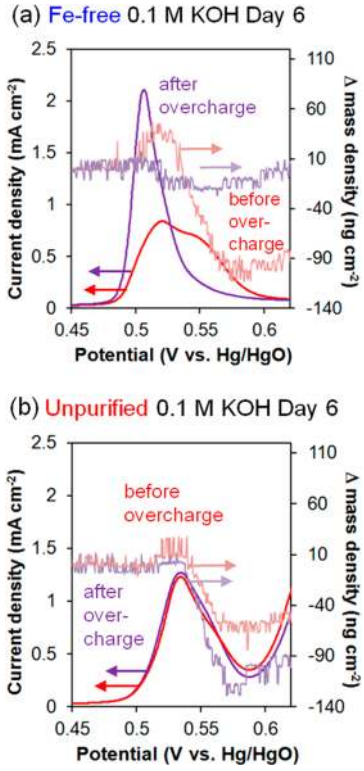

Figure 10. QCM mass density change with concurrent 10 mV s^{-1} potential scans for $Ni(OH)_2$ films deposited on Au/Ti quartz crystals in (a) Fe-free and (b) unpurified 0.1 M KOH (both after 6 days of aging in 1 M KOH). Cycles are shown before and after the 10 mV s^{-1} overcharge scan to 0.85 V. The oxygen evolution equilibrium potential is 0.365 V vs Hg/HgO in 0.1 M KOH.

For the $Ni(OH)_2$ film aged in unpurified KOH electrolyte, minimal differences are observed between the CVs before and after an overcharge cycle to 0.85 V. After overcharge, the QCM mass density decreases slightly compared with the prior oxidation cycle, possibly as a result of oxygen bubble formation on the quartz crystal surface.

4. DISCUSSION

4.1. $Ni(OH)_2$/NiOOH Structural Changes with Aging and Overcharging in Fe-Free KOH. Although the transformation of α-$Ni(OH)_2$ to β-$Ni(OH)_2$ with aging has been reported previously, all earlier observations were likely carried

DOI: 10.1021/acs.jpcc.5b00105
J. Phys. Chem. C 2015, 119, 7243−7254

out in KOH contaminated with Fe, and therefore, the results may have been unintentionally convoluted with the effects of Fe accumulation in the sample.[25,28] The Raman feature observed in this work at 453 cm^{-1} is consistent with that of lattice vibrations of β-$Ni(OH)_2$ (445−449 cm^{-1})[6,8,39,40] or α-$Ni(OH)_2$ (460−465 cm^{-1})[8,39] and thus could indicate the presence of either phase. The feature seen at 490 cm^{-1}, also observed at low potentials, has previously been assigned to a Ni−O vibration present in defective or disordered Ni-$(OH)_2$.[8,24,41,42] Commercially available, crystalline β-$Ni(OH)_2$ is isostructural to brucite, whereas α-$Ni(OH)_2$ is described as planes of β-$Ni(OH)_2$ intercalated with water.[39,43,44] However, additional structural variations can occur as a result of hydration and structural defects.[43,44]

The γ-NiOOH and β-NiOOH phases are also structurally similar, with the larger sheet spacing between the γ-NiOOH layers being the primary difference between these phases. The Raman features at 476−477 cm^{-1} and 555−560 cm^{-1}, present at higher potentials, are ascribed to Ni−O vibrations of NiOOH; both the γ- and β-NiOOH phases are reported to exhibit Raman features at these wavenumbers.[6,8,25,39]

Raman spectra of α-$Ni(OH)_2$ are expected to be similar to those of β-$Ni(OH)_2$, since there is an increase only in the c-axis of the unit cell (due to a larger intersheet spacing) and no major change in crystal symmetry.[39] Within mixed phase samples, the overlap of Raman features at low wavenumbers creates further difficulty in distinguishing these phases.[44] Since the low-frequency modes of α- and β-$Ni(OH)_2$ are difficult to differentiate, features observed in the O−H stretching region (3000−3800 cm^{-1}) provide an additional basis for discrimination between α- and β-$Ni(OH)_2$. The characteristic O−H stretch for β-$Ni(OH)_2$ is expected at 3581 cm^{-1},[8,24,44] whereas that for α-$Ni(OH)_2$ is reported at ∼3660 cm^{-1}.[8,44] The broad features observed at 3000−3600 cm^{-1} are characteristic of water.[8]

The results presented above demonstrate that $Ni(OH)_2$ does, indeed, undergo structural transformation upon aging in Fe-free KOH. As-deposited $Ni(OH)_2$ is present as α-$Ni(OH)_2$, as evidenced by the Raman stretching mode ν(O−H), observed at 3665 cm^{-1} at 0.2 V. Further evidence for the presence of α-$Ni(OH)_2$ prior to aging is given by the change in sample mass, measured by QCM, before and after oxidation (Figure 10a). For the day 0 sample, the α-$Ni(OH)_2$-to-γ-NiOOH conversion results in a ∼160 ng cm^{-2} increase in mass due to ion intercalation upon oxidation.

After a day or more of aging, the presence of the 3581 cm^{-1} Raman peak is characteristic of a β-$Ni(OH)_2$ phase. We note that the 3581 cm^{-1} feature is much weaker than that recorded for crystalline β-$Ni(OH)_2$,[8,24] indicating structural disorder within this phase. The transformation of α-$Ni(OH)_2$ to β-$Ni(OH)_2$ is also observed in QCM measurements: after 6 days of aging, a ∼110 ng cm^{-2} mass *decrease* with oxidation occurs, a mass loss generally attributed to proton extraction from β-$Ni(OH)_2$ to form β-NiOOH.[27,38,45] Previous investigations have also confirmed the QCM mass change (mass increase for α/γ vs mass decrease for β/β with oxidation) tracks with the structural transformation of α-$Ni(OH)_2$ to β-$Ni(OH)_2$, observed via X-ray diffraction.[45]

The aging phase transformation in Fe-free KOH is also accompanied by several changes in the voltammograms presented in Figure 2a. Since minimal change occurs in the NiOOH → $Ni(OH)_2$ reduction peak position, consistent with previous reports,[46] we focus our discussion on the oxidation features. With increasing days of aging, the 0.43 V oxidation wave shifts anodically and decreases in intensity; this wave is attributed to the oxidation of α-$Ni(OH)_2$ to γ-NiOOH. After aging, an additional oxidation wave appears at ∼0.47 V, which is primarily attributed to the oxidation of β-$Ni(OH)_2$ to β-NiOOH. This shift is similar to that reported previously for aging of $Ni(OH)_2$ films in Fe-free KOH and is in line with the Bode model, which reports that $\alpha \rightarrow \gamma$ conversion should occur at a lower potential than $\beta \rightarrow \beta$ conversion.[5,28,30] However, these phases are structurally disordered and intermediate phases between α/γ and β/β could exist, which could produce additional main oxidation wave contributions, such as that observed for day 1 in Fe-free electrolyte. We note that in Figure 2a, potentials in excess of the "overcharging" potential (∼0.75 V) are scanned, producing a mixture of the α/γ and β/β phases even after 6 days of aging. However, only one primary oxidation wave is apparent after 6 days of aging due to α-$Ni(OH)_2$ oxidation to γ-NiOOH overlapping with β-$Ni(OH)_2$ oxidation to β-NiOOH (see the further discussion in SI 11). It appears that the formation of β/β impedes the oxidation of α/γ, resulting in the anodic shift of α-$Ni(OH)_2$ to γ-NiOOH oxidation and the merging of these two previously distinct oxidation waves.

For samples maintained below 0.7 V during 6 days of aging in 1 M Fe-free KOH, "overcharging" of NiOOH to 0.85 V produces clear changes in the voltammograms: the main oxidation wave shifts to lower potentials, and two additional oxidation features become apparent over the roughened Au Raman electrode, which has a 2−2.5 times thinner film of $Ni(OH)_2$ compared with the QCM samples (Figure 9 vs Figure 10 and SI Figure S11.1). The 30 mV cathodic shift of the main oxidation waves after overcharging in Figure 9 contrasts with the 30−60 mV anodic shift of the main oxidation wave observed after aging in Figure 8a, suggesting that overcharging reverses the effects of aging (i.e., overcharging converts β/β back to α/γ). The smaller 0.60/0.66 V oxidation feature observed in 0.1 M KOH/1 M KOH is present on day 0 (Figure 2a) as well as after overcharging (Figure 9); this smaller wave accompanies the main, as-deposited oxidation wave. We thus propose that this oxidation feature is related to the γ-NiOOH phase, perhaps as the formation of some higher oxidation state Ni^{IV}. Meanwhile, the 0.7/0.76 V oxidation peak is strongest on the initial overcharge cycle and corresponds to a QCM mass increase (Supporting Information Section S12); we therefore attribute it to the overcharge conversion of β-NiOOH to γ-NiOOH. This oxidation current could be due to an increase in the average Ni oxidation state; the average oxidation state of Ni in γ-NiOOH is reported to be 3.3−3.7, whereas the average oxidation state of Ni within β-NiOOH is estimated to be 2.7−3.0.[5,7,34,47]

Because the frequency of a vibrational mode is proportional to bond strength, a decrease in the average nickel oxidation state after aging γ-NiOOH to β-NiOOH is expected to decrease the band frequency.[6] This is consistent with a slight shift in the NiOOH features after aging to lower wavenumbers (477 to 476 cm^{-1} and 560 to 558 cm^{-1}). However, Raman peak intensities are expected to be more sensitive than the peak frequencies; relative peak intensities can vary on the basis of local structural disorder, hydrogen and vacancy content, and nickel oxidation state.[8] Previous investigations have found that the 480 cm^{-1}/560 cm^{-1} Raman peak height ratio is significantly lower for β-NiOOH than for γ-NiOOH.[8,25]

DOI: 10.1021/acs.jpcc.5b00105
J. Phys. Chem. C 2015, 119, 7243−7254

We investigated the Raman peak ratio as a function of applied potential before and after 6 days of aging in the absence (and presence, to be discussed in the following section) of Fe electrolyte impurities (Supporting Information Figure S9.4); the results are summarized in Table 1. In Fe-free KOH, this ratio is initially ~1.4 after the onset of NiOOH formation at 0.47 V and stabilizes at 1.55 after the $Ni(OH)_2$ oxidation wave (above 0.52 V). Films aged for 6 days in Fe-free electrolyte follow the same trend with an overall lower ratio, 1.25 increasing to 1.42 with further oxidation (above 0.54 V). The lower peak ratio after aging is evidence for conversion of the film from α/γ to β/β with aging.

Table 1. NiOOH 480 cm^{-1}/560 cm^{-1} Raman Peak-Height Ratio at 0.6 V in 0.1 M KOH

	day 0	day 6 (after aging)	day 6 (after overcharging)
Fe-free KOH	1.55	1.42	1.48
unpurified KOH	1.55	1.28	*a*

[a]Because of extensive oxygen bubble formation with overcharging in unpurified electrolyte, subsequent Raman acquisitions "after overcharging" were not completed.

The ratio of these Raman peak intensities was also calculated after the overcharging cycle to 0.85 V for the aged sample. The 480/560 cm^{-1} ratio increased from 1.42 for the aged sample to 1.48 after the overcharging sweep to 0.85 V, suggesting that a more γ-like NiOOH structure is formed after overcharging (although this increased ratio is still less than the 1.55 ratio observed on day 0). This intermediate peak-height ratio of 1.48 indicates that after overcharging, a mixture of γ- and β-NiOOH is present under OER conditions, that is, the film does not return *completely* to its original, as-deposited α/γ state with the peak ratio of 1.55. The appearance of two main oxidation waves in the voltammograms after overcharging (Figure 9) also supports that both α- and β-$Ni(OH)_2$ phases are present and oxidize to their respective γ- and β-NiOOH phases, whereas in the cycles before overcharging, the β-$Ni(OH)_2$ phase is predominantly present and oxidizes to β-NiOOH. The QCM frequency change at the primary oxidation wave after overcharging (Figure 10a) is between that of the day 0 and day 6 oxidation waves (Figure 8a), further confirming that a mixture of the γ-NiOOH and β-NiOOH phases exists after overcharging.

After overcharging, some amount of α-$Ni(OH)_2$/γ-NiOOH reconverts (i.e., ages) to β-$Ni(OH)_2$/β-NiOOH on the time scale of minutes if maintained below 0.7 V. This conversion is clearly observable within slow (1 mV s^{-1}) voltammograms completed with concurrent Raman acquisitions (~20 min/cycle, Figure S11.1 SI) but not during the faster, 10 mV s^{-1} CVs (~2 min/cycle) shown in Figure 9. The occurrence of the small oxidation wave at 0.7 V in the RDE voltammograms after aging (Figure 2a) is further evidence that a small amount of β-NiOOH is reconverted to γ-NiOOH with each anodic potential scan.

In summation, despite previous reports examining $Ni(OH)_2$/NiOOH phase changes using electrolytes containing Fe impurities, structural changes observed after aging and overcharging in Fe-free electrolyte closely align with the commonly accepted structural transformation scheme previously detailed by Bode.[28] The work here represents the first time that detailed structural information in the Ni-(oxy)-hydroxides has been examined under rigorously Fe-free conditions and definitively shows that structural transformations between the α/γ and β/β couples are inherent to the Ni-(oxy)hydroxides themselves and not simply a byproduct of Fe-impurity incorporation.

4.2. $Ni(OH)_2$/NiOOH Structural Changes with Aging and Overcharging in Unpurified KOH. Aging of $Ni(OH)_2$ in unpurified (Fe-containing) KOH produces electrochemical and structural changes distinct from those observed after aging in Fe-free KOH, although the overall film is found to maintain a $Ni(OH)_2$/NiOOH-type structure. This conclusion is consistent with the work of Friebel et al., which showed that codeposited Ni−Fe films containing <25% Fe content were also structurally characteristic of $Ni(OH)_2$/NiOOH.[29] For $Ni(OH)_2$ films aged in unpurified electrolyte, the development of a second main oxidation feature is not as clearly defined, but an even greater shift (70 mV vs 40 mV in Fe-free KOH) in the primary oxidation/reduction waves is observed (Figure 2b). This shift is primarily due to the incorporation of Fe impurities; Fe addition is well known to shift the main oxidation/reduction waves to more anodic potentials.[10−12,18,24]

After extended exposure to Fe impurities, additional changes are observed in the $Ni(OH)_2$/NiOOH structure. Although some amount of β-NiOOH is formed after aging in unpurified electrolyte, it is clearly less than the amount formed in Fe-free electrolyte. This difference can be seen in both the 50 ng cm^{-2} QCM mass decrease with oxidation (Figure 8) (which is less than the ~110 ng cm^{-2} decrease observed in films aged in Fe-free electrolyte) as well as a less intense 3580 cm^{-1} Raman feature (Figure 7) after aging in unpurified KOH.

Additional Raman spectra differences indicate further NiOOH structural changes unique to the incorporation of Fe impurities. The ratio of 480/560 cm^{-1} Raman peak intensities in unpurified electrolyte is initially (day 0) comparable to that observed without Fe impurities (initially 1.3 at 0.45 V, stabilizing at 1.55 above 0.52 V), but after 6 days of aging, a distinct difference is observed. The ratio, 1.33 with initial NiOOH formation at ~0.5 V, further decreases with the Ni(II)/Ni(III) oxidation wave, reaching 1.28 at 0.6 V.

A greater reduction in the 480/560 cm^{-1} Raman peak height ratio as well as a broadening of these features is observed for $Ni(OH)_2$ films aged in unpurified electrolyte compared with those aged in Fe-free KOH (Table 1 and SI Figure S9.1). These differences cannot be solely due to greater β-NiOOH formation in the unpurified electrolyte, because as previously noted, QCM results show that less β-NiOOH is formed in the presence of Fe impurities. In addition, various iron phases, including α-FeOOH and Fe_3O_4, are expected to have other Raman-active modes below 800 cm^{-1},[48] which are not observed in our current study. Therefore, this change in Raman peak-height ratio with aging in the presence of Fe impurities must be the result of Fe incorporation. X-ray diffraction studies have shown that $Ni(OH)_2$ codeposited with 25% Fe can generate a Ni−Fe layered-double-hydroxide (NiFe-LDH) structure.[30] Previous Raman studies also evidenced broader 480 and 560 cm^{-1} intensities, as well as a lower 480/560 ratio, for an oxidized NiFe-LDH compared with pure NiOOH.[49] Therefore, we attribute the further decrease of the 480/560 cm^{-1} ratio after aging in unpurified KOH to the formation of NiFe-LDH, which is produced by substitution of Fe impurities into the $Ni(OH)_2$/NiOOH lattice.

In unpurified KOH, the formation of the NiFe-LDH phase is also in line with the overcharging differences observed between Fe-free vs unpurified KOH samples. The minimal mass change

DOI: 10.1021/acs.jpcc.5b00105
J. Phys. Chem. C 2015, 119, 7243−7254

observed before and after overcharge in unpurified KOH (Figure 10b) is a result of less β-$Ni(OH)_2$ formation due to the presence of the NiFe-LDH, indicating that the NiFe-LDH phase inhibits the conversion of α/γ to β/β. This inhibition of conversion to the β-$Ni(OH)_2/\beta$-NiOOH phase with aging was also recently observed for codeposited NiFe-LDH.[30]

Figure 11 illustrates how the current density and normalized intensity of the Raman band at 560 cm^{-1} (an indicator of NiOOH formation) change with applied potential. The oxidation wave is comparable for both Fe-free and unpurified electrolyte on day 0, but the transformation of $Ni(OH)_2$ to NiOOH, as observed by the formation of the 560 cm^{-1} band, exhibits a sharper onset when oxidation occurs in Fe-free electrolyte.

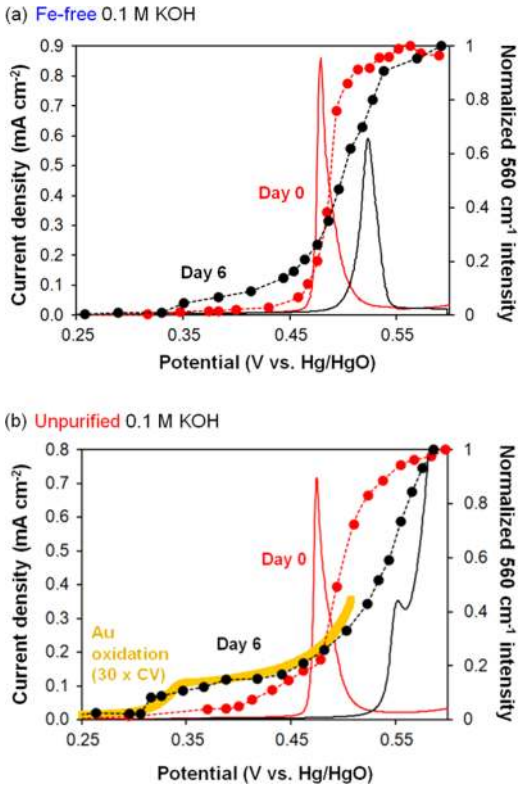

Figure 11. Normalized 560 cm^{-1} Raman intensity (an indicator of NiOOH formation) and concurrent 1 mV s^{-1} linear potential scans for $Ni(OH)_2$ films deposited on roughened Au in (a) Fe-free and (b) unpurified 0.1 M KOH before (red) and after (black) aging in 1 M KOH. The Au oxidation voltammogram wave is shown 30 × for reference in (b). Oxygen evolution equilibrium potential is 0.365 V vs Hg/HgO in 0.1 M KOH.

After aging for 6 days in unpurified KOH, the $Ni(OH)_2$/NiOOH oxidation wave shifts to significantly higher potentials compared with what is observed in Fe-free electrolyte. However, for both purified and unpurified electrolyte, NiOOH begins to form at potentials 0.1−0.2 V below the onset of the electrochemical Ni(II)/Ni(III) oxidation wave (~0.35 V). This initial NiOOH formation tracks with the onset of Au oxidation (shown for the sample in unpurified KOH in Figure 11b). Although Au oxide has a broad feature at 570 cm^{-1},[33] the parallel emergence of the feature at 480 cm^{-1} confirms assignment of this mode to NiOOH. It has been shown that both the Au substrate and codeposited Fe can exert charge-transfer effects to partially oxidize $Ni(OH)_2$.[25,30] After aging, stronger charge-transfer effects could result from the formation of a Au/Ni surface alloy. Such an alloy has been shown to form at room temperatures, and evidence for a mixed Au/Ni oxide or hydroxide has also been observed for thin Ni films (<5 monolayers) electrodeposited over Au.[25,50,51] Therefore, we propose a small amount of a NiOOH-type structure is formed with the onset of bulk Au oxidation after aging due to intermixing of Ni and Au at the substrate interface. We note, however, that this interfacial NiOOH likely produces disproportionately strong Raman intensities at 480/560 cm^{-1} as a result of strong surface-enhancement effects for the few monolayers of $Ni(OH)_2$/NiOOH closest to the Au substrate.

In summary, aging $Ni(OH)_2$ films in the presence of Fe impurities produces structural changes distinct from those changes which occur in Fe-free electrolyte. In contrast to films aged in Fe-free KOH, the primary structural change after aging in the presence of Fe impurities is the incorporation of Fe within the Ni-(oxy)hydroxide structure to produce a NiFe-LDH. This phase is found to inhibit the aging formation of β-$Ni(OH)_2/\beta$-NiOOH as well as the overcharging conversion of β-NiOOH to γ-NiOOH, both of which are significant deviations from the Bode scheme.

4.3. Effect of NiOOH Structure and Fe Incorporation on OER Activity. We next relate the OER activities of Ni-(oxy)hydroxide films to the corresponding structural changes observed before and after aging in the absence and presence of iron impurities in KOH electrolyte. The as-deposited γ-NiOOH free of Fe contamination is not very active for the OER, exhibiting an overpotential of 525 mV at 10 mA cm^{-2} (1 M KOH). As more β-NiOOH is formed, the overpotential rises to 620 mV. Furthermore, the Tafel slope for the OER is lower for the as-prepared samples (105 mV dec^{-1}) than for the aged samples (135 mV dec^{-1}). For all samples cycled in Fe-free electrolyte, both the γ-NiOOH and β-NiOOH phases exhibit extremely poor oxygen evolution activity, and the aged films (with more β-NiOOH) appear to be worse OER catalysts. However, it must be noted that this potential (0.926 V vs Hg/HgO) is well above the 0.7 V vs Hg/HgO overcharging potential, so some amount of γ-NiOOH will be present (in addition to β-NiOOH) under OER conditions in Fe-free electrolyte. Therefore, we cannot say definitively that *pure* β-NiOOH displays lower OER activity than pure γ-NiOOH.

Consistent with previous findings, Fe impurities present at <1 ppm in the KOH electrolyte spontaneously incorporate into $Ni(OH)_2$/NiOOH films and significantly enhance the OER activity.[30] Maximum oxygen evolution activity occurs at approximately 12−17% Fe content (Figure 5), attained after 5 days of aging. It is notable that the maximum activity achieved as a result of aging is comparable to that reported after intentional Fe addition to Ni-(oxy)hydroxide (j = 20 mA cm^{-2} at η = 300 mV and η = 280 mV at j = 10 mA cm^{-2} at 40 at. % Fe).[24]

Although the overpotential at j = 10 mA cm^{-2} does not exhibit improvement above Fe contents of 17%, Fe incorporates in excess of 25% after extended aging in unpurified 1 M KOH, as determined from elemental analysis (Figure 3). In addition, comparable Fe film contents calculated from both XPS (surface) and ICP (bulk) techniques show that Fe incorporates throughout the entire $Ni(OH)_2$ film, in agreement with previous work by Corrigan,[10] as well as Trotochaud et al.[30]

X-ray absorption spectroscopy (XAS) studies by Friebel et al. have shown that for mixed Ni−Fe oxyhydroxides, it is Fe^{3+} incorporated into a γ-NiOOH-like structure that displays

DOI: 10.1021/acs.jpcc.5b00105
J. Phys. Chem. C 2015, 119, 7243−7254

enhanced OER activity.[29] The authors suggest that this high activity arises as a result of the bond contraction of Fe−O, measured to be 7% shorter than in γ-FeOOH, which occurs after the host $Ni(OH)_2$ oxidizes to NiOOH. Density-functional theory calculations confirm that Fe sites present within the NiOOH structure exhibit more optimal adsorption energies of proposed OER intermediates (OH, O, OOH), thereby reducing the required overpotential for this reaction.

Figure 12 plots the turnover frequency (TOF, at η = 300 mV) on a per-Fe-site basis versus Fe content. Iron sites were calculated as the total number of Fe atoms determined from ICP or XPS. The TOF is lower (~3 s^{-1}) for low Fe content, maximizes at 3−4 days of aging (~11% Fe content, close to the 12% Fe estimated from XPS for maximum activity), and then decreases with continued aging. The lower TOF after initial cycling and aging could be due to the Fe atoms (1) not initially incorporating within the NiOOH structure, (2) first incorporating within the NiOOH structure at locations that are less OER-active, (3) existing at too low a concentration within the NiOOH lattice to be optimally active (e.g., a minimum density of neighboring Fe sites could produce higher activity), or (4) incorporating into differing Ni structures with aging due to the concurrent partial transformation of α-$Ni(OH)_2$/γ-NiOOH to β-$Ni(OH)_2$/β-NiOOH.

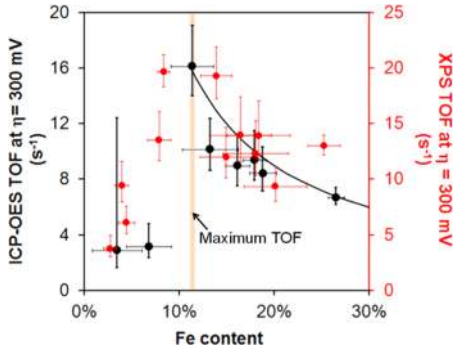

Figure 12. Turnover frequency (calculated on a per-Fe site basis) from total Fe content (ICP-OES: black, XPS: red) for $Ni(OH)_2$ films deposited on polished Au RDEs as a function of Fe content. Solid line represents anticipated TOF assuming Fe content exceeding 11% is not OER-active. Error bars indicate the inherent uncertainty in the Fe content as determined by ICP-OES and XPS for each sample. See S13 for a complete discussion of error calculation.

The TOF decrease after exceeding 11% Fe content could be due to the NiOOH phase reaching critical saturation and the formation of a separate, inactive Fe-rich phase. The dashed line in Figure 12 estimates the TOF assuming the formation of such an inactive phase, where any additional Fe sites added (past 11% Fe) are not OER-active (for calculation, see Supporting Information). These anticipated values closely track calculated TOFs at Fe = 11−28% and support that Fe present within the NiOOH structure are the active sites for the OER, and at higher Fe content, Fe incorporates into less OER-active Fe-rich phases.

Consistent with this hypothesis, Friebel et al.[29] observe direct XAS evidence that a separate, Fe-rich phase forms within Ni−Fe catalyst films at higher Fe contents (>25%), and OER activity decreases as this less active phase predominates. We note that differences between this "Fe saturation limit" estimated in the current work (11% Fe) vs that of Friebel et al. (25% Fe) could be due to differences in sample preparation or aging. In contrast with our current study of Fe-impurity uptake within $Ni(OH)_2$/NiOOH films, Friebel et al. investigated codeposited Ni−Fe films. It is also possible that in the previous study, an Fe-rich phase formed at Fe contents below 25% but remained below detection limits of XAS. In the present study, we do not observe direct structural evidence for a separate, Fe-rich phase after 6 days of aging, which is not incongruous with a disordered Fe phase exhibiting limited long-range order.

5. CONCLUSIONS

Electrochemical characterization, in situ Raman spectroscopy, and quartz crystal microbalance measurements were used to differentiate the effects of structural changes vs Fe incorporation after aging $Ni(OH)_2$/NiOOH films in KOH. Ni hydroxide films aged in unpurified electrolyte incorporate > 20% Fe after 5 weeks of aging in 1 M unpurified, reagent-grade KOH. In addition, samples aged in unpurified electrolyte exhibit a much higher activity and lower overpotential, as well as a significantly lower Tafel slope, compared with samples aged in Fe-free KOH. Optimum catalyst activity, observed after 5 days of aging in unpurified 1 M KOH, is comparable to optimized activities reported for NiOOH catalysts with intentional Fe addition. Conversely, Fe-free films exhibit very poor activity, which further decreases with aging. $Ni(OH)_2$ aged in Fe-free electrolyte is mostly characteristic of disordered β-$Ni(OH)_2$. In line with the Bode scheme, overcharging occurs above 0.7 V in 1 M Fe-free KOH (0.76 V in 0.1 M KOH), coinciding with a large, secondary oxidation wave. After cycling to 0.85 V, β-NiOOH reconverts to γ-NiOOH in Fe-free electrolyte. In contrast, films aged in unpurified KOH evidence less phase transformation after aging and overcharging but do incorporate Fe impurities to form a NiFe-layered double (oxy)hydroxide structure. Turnover frequency comparisons, calculated on a per-Fe site basis, support that Fe within the NiOOH structure is the OER active site, and for Fe contents exceeding ~11%, a separate, Fe-rich phase begins to form. These findings further elucidate the effects of Fe impurity incorporation on the Ni-(oxy)hydroxide catalyst structure and OER activity, which is critical for high OER activity over these materials.

■ ASSOCIATED CONTENT

Supporting Information

Additional experimental procedures, supplementary electrochemical data and calculations. This material is available free of charge via the Internet at http://pubs.acs.org.

■ AUTHOR INFORMATION

Corresponding Author

*E-mail: bell@cchem.berkeley.edu.

Notes

The authors declare no competing financial interest.

■ ACKNOWLEDGMENTS

This material is based upon work performed by the Joint Center for Artificial Photosynthesis, a DOE Energy Innovation Hub, supported through the Office of Science of the U.S. Department of Energy under Award No. DE-SC0004993. The authors gratefully acknowledge Eric Granlund (University of California, Berkeley, College of Chemistry) for Raman electrochemical cell fabrication, as well as James Wu and

DOI: 10.1021/acs.jpcc.5b00105
J. Phys. Chem. C 2015, 119, 7243−7254

Doug Jamieson (Lawrence Berkeley National Laboratory, Materials Science Division) for RDE fabrication. The authors also thank Elena Kreimer (University of California, Berkeley, College of Chemistry) for assistance with elemental analysis training, as well as Jason Cooper and Ian Sharp (Joint Center for Artificial Photsynthesis) for XPS assistance.

REFERENCES

(1) Cook, T. R.; Dogutan, D. K.; Reece, S. Y.; Surendranath, Y.; Teets, T. S.; Nocera, D. G. Solar Energy Supply and Storage for the Legacy and Non Legacy Worlds. *Chem. Rev.* **2010**, *110*, 6474−6502.
(2) Walter, M. G.; Warren, E. L.; McKone, J. R.; Boettcher, S. W.; Mi, Q.; Santori, E. A.; Lewis, N. S. Solar Water Splitting Cells. *Chem. Rev.* **2010**, *110*, 6446−6473.
(3) Suntivich, J.; May, K. J.; Gasteiger, H. A.; Goodenough, J. B.; Shao-Horn, Y. A Perovskite Oxide Optimized for Oxygen Evolution Catalysis from Molecular Orbital Principles. *Science* **2011**, *334*, 1383−1385.
(4) Hall, D. E. $Ni(OH)_2$-Impregnated Anodes for Alkaline Water Electrolysis. *J. Electrochem. Soc.* **1983**, *130*, 317−321.
(5) Lyons, M. E. G.; Brandon, M. P. The Oxygen Evolution Reaction on Passive Oxide Covered Transition Metal Electrodes in Aqueous Alkaline Solution. Part 1-Nickel. *Int. J. Electrochem. Soc.* **2008**, *3*, 1386−1424.
(6) Cornilsen, B. C.; Karjala, P. J.; Loyselle, P. L. Structural Models for Nickel Electrode Active Mass. *J. Power Sources* **1988**, *22*, 351−357.
(7) Desilvestro, J.; Corrigan, D. A.; Weaver, M. J. Characterization of Redox States of Nickel-Hydroxide Film Electrodes by In Situ Surface Raman-Spectroscopy. *J. Electrochem. Soc.* **1988**, *135*, 885−892.
(8) Kostecki, R.; McLarnon, F. Electrochemical and In Situ Raman Spectroscopic Characterization of Nickel Hydroxide Electrodes. *J. Electrochem. Soc.* **1997**, *144*, 485−493.
(9) Bediako, D. K.; Lassalle-Kaiser, B.; Surendranath, Y.; Yano, J.; Yachandra, V. K.; Nocera, D. G. Structure-Activity Correlations in a Nickel-Borate Oxygen Evolution Catalyst. *J. Am. Chem. Soc.* **2012**, *134*, 6801−6809.
(10) Corrigan, D. A. The Catalysis of the Oxygen Evolution Reaction by Iron Impurities in Thin-Film Nickel-Oxide Electrodes. *J. Electrochem. Soc.* **1987**, *134*, 377−384.
(11) Li, X. H.; Walsh, F. C.; Pletcher, D. Nickel Based Electrocatalysts for Oxygen Evolution in High Current Density, Alkaline Water Electrolysers. *Phys. Chem. Chem. Phys.* **2011**, *13*, 1162−1167.
(12) Singh, R. N.; Pandey, J. P.; Anitha, K. L. Preparation of Electrodeposited Thin-Films of Nickel Iron-Alloys on Mild-Steel for Alkaline Water Electrolysis. 1. Studies on Oxygen Evolution. *Int. J. Hydrogen Energy* **1993**, *18*, 467−473.
(13) Trotochaud, L.; Ranney, J. K.; Williams, K. N.; Boettcher, S. W. Solution-Cast Metal Oxide Thin Film Electrocatalysts for Oxygen Evolution. *J. Am. Chem. Soc.* **2012**, *134*, 17253−17261.
(14) Gong, M.; Li, Y.; Wang, H.; Liang, Y.; Wu, J. Z.; Zhou, J.; Wang, J.; Regier, T.; Wei, F.; Dai, H. An Advanced Ni-Fe Layered Double Hydroxide Electrocatalyst for Water Oxidation. *J. Am. Chem. Soc.* **2013**, *135*, 8452−8455.
(15) McCrory, C. C. L.; Jung, S. H.; Peters, J. C.; Jaramillo, T. F. Benchmarking Heterogeneous Electrocatalysts for the Oxygen Evolution Reaction. *J. Am. Chem. Soc.* **2013**, *135*, 16977−16987.
(16) Landon, J.; Demeter, E.; Inoglu, N.; Keturakis, C.; Wachs, I. E.; Vasic, R.; Frenkel, A. I.; Kitchin, J. R. Spectroscopic Characterization of Mixed Fe−Ni Oxide Electrocatalysts for the Oxygen Evolution Reaction in Alkaline Electrolytes. *ACS Catal.* **2012**, *2*, 1793−1801.
(17) Miller, E. L.; Rocheleau, R. E. Electrochemical Behavior of Reactively Sputtered Iron-Doped Nickel Oxide. *J. Electrochem. Soc.* **1997**, *144*, 3072−3077.
(18) Hu, C. C.; Wu, Y. R. Bipolar Performance of the Electroplated Iron-Nickel Deposits for Water Electrolysis. *Mater. Chem. Phys.* **2003**, *82*, 588−596.
(19) Smith, R. D. L.; Prevot, M. S.; Fagan, R. D.; Zhang, Z. P.; Sedach, P. A.; Siu, M. K. J.; Trudel, S.; Berlinguette, C. P. Photochemical Route for Accessing Amorphous Metal Oxide Materials for Water Oxidation Catalysis. *Science* **2013**, *340*, 60−63.
(20) Smith, R. D. L.; Prévot, M. S.; Fagan, R. D.; Trudel, S.; Berlinguette, C. P. Water Oxidation Catalysis: Electrocatalytic Response to Metal Stoichiometry in Amorphous Metal Oxide Films Containing Iron, Cobalt, and Nickel. *J. Am. Chem. Soc.* **2013**, *135*, 11580−11586.
(21) Merrill, M. D.; Dougherty, R. C. Metal Oxide Catalysts for the Evolution of O_2 from H_2O. *J. Phys. Chem. C* **2008**, *112*, 3655−3666.
(22) Cappadonia, M.; Divisek, J.; Vonderheyden, T.; Stimming, U. Oxygen Evolution at Nickel Anodes in Concentrated Alkaline-Solution. *Electrochim. Acta* **1994**, *39*, 1559−1564.
(23) Lu, P. W. T.; Srinivasan, S. Electrochemical-Ellipsometric Studies of Oxide Film Formed on Nickel during Oxygen Evolution. *J. Electrochem. Soc.* **1978**, *125*, 1416−1422.
(24) Louie, M. W.; Bell, A. T. An Investigation of Thin-Film Ni−Fe Oxide Catalysts for the Electrochemical Evolution of Oxygen. *J. Am. Chem. Soc.* **2013**, *135*, 12329−12337.
(25) Yeo, B. S.; Bell, A. T. In Situ Raman Study of Nickel Oxide and Gold-Supported Nickel Oxide Catalysts for the Electrochemical Evolution of Oxygen. *J. Phys. Chem. C* **2012**, *116*, 8394−8400.
(26) Godwin, I. J.; Lyons, M. E. G. Enhanced Oxygen Evolution at Hydrous Nickel Oxide Electrodes via Electrochemical Ageing in Alkaline Solution. *Electrochem. Commun.* **2013**, *32*, 39−42.
(27) Wehrens-Dijksma, M.; Notten, P. H. L. Electrochemical Quartz Microbalance Characterization of Ni(OH)(2)-Based Thin Film Electrodes. *Electrochim. Acta* **2006**, *51*, 3609−3621.
(28) Bode, H.; Dehmelt, K.; Witte, J. Zur Kenntnis der Nickel-hydroxidelektrode—I.Über Das Nickel (II)-Hydroxidhydrat. *Electrochim. Acta* **1966**, *11*, 1079−1087.
(29) Friebel, D.; Louie, M. W.; Bajdich, M.; Sanwald, K. E.; Cai, Y.; Wise, A. M.; Cheng, M. J.; Sokaras, D.; Weng, T. C.; Alonso-Mori, R.; Davis, R. C.; Bargar, J. R.; Norskov, J. K.; Nilsson, A.; Bell, A. T. Identification of Highly Active Fe Sites in (Ni,Fe)OOH for Electrocatalytic Water Splitting. *J. Am. Chem. Soc.* **2015**, *137*, 1305−1313.
(30) Trotochaud, L.; Young, S. L.; Ranney, J. K.; Boettcher, S. W. Nickel-Iron Oxyhydroxide Oxygen-Evolution Electrocatalysts: The Role of Intentional and Incidental Iron Incorporation. *J. Am. Chem. Soc.* **2014**, *136*, 6744−6753.
(31) Gao, P.; Gosztola, D.; Leung, L. W. H.; Weaver, M. J. J. Surface-Enhanced Raman-Scattering at Gold Electrodes − Dependence on Electrochemical Pretreatment Conditions and Comparisons with Silver. *Electroanal. Chem.* **1987**, *233*, 211−222.
(32) Sauerbrey, G. Z. Verwendung Von Schwingquarzen Zur Wagung Dunner Schichten Und Zur Mikrowagung. *Z. Phys.* **1959**, *155*, 206−222.
(33) Yeo, B. S.; Klaus, S. L.; Ross, P. N.; Mathies, R. A.; Bell, A. T. Identification of Hydroperoxy Species as Reaction Intermediates in the Electrochemical Evolution of Oxygen on Gold. *ChemPhysChem* **2010**, *11*, 1854−1857.
(34) Oliva, P.; Leonardi, J.; Laurent, J. F.; Delmas, C.; Braconnier, J. J.; Figlarz, M.; Fievet, F.; Deguibert, A. Review of the Structure and the Electrochemistry of Nickel Hydroxides and Oxy-Hydroxides. *J. Power Sources* **1982**, *8*, 229−255.
(35) Plyasunova, N. V.; Zhang, Y.; Muhammed, M. Critical Evaluation of Thermodynamics of Complex Formation of Metal Ions in Aqueous Solutions. IV. Hydrolysis and hydroxo-complexes of Ni^{2+} at 298.15 K. *Hydrometallurgy* **1998**, *41*, 43−63.
(36) Lyons, M. E. G.; Brandon, M. P. A Comparative Study of the Oxygen Evolution Reaction on Oxidised Nickel, Cobalt and Iron Electrodes in Base. *J. Electroanal. Chem.* **2010**, *641*, 119−130.
(37) Dechialvo, M. R. G.; Chialvo, A. C. Oxygen Evolution Reaction on Thick Hydrous Nickel-Oxide Electrodes. *Electrochim. Acta* **1988**, *33*, 825−830.

DOI: 10.1021/acs.jpcc.5b00105
J. Phys. Chem. C 2015, 119, 7243−7254

(38) Lee, J. W.; Han, J. H.; Seo, M.; Pyun, S. Transport of alkaline cation and neutral species through the alpha-Ni(OH)(2)/γ-NiOOH film electrode. *J. Solid State Electrochem.* **2001**, *5*, 459−465.
(39) Johnston, C.; Graves, P. R. In Situ Raman-Spectroscopy Study of the Nickel Oxyhydroxide Electrode (NOE) System. *Appl. Spectrosc.* **1990**, *44*, 105−115.
(40) Bantignies, J. L.; Deabate, S.; Righi, A.; Rols, S.; Hermet, P.; Sauvajol, J. L.; Henn, F. New Insight into the Vibrational Behavior of Nickel Hydroxide and Oxyhydroxide Using Inelastic Neutron Scattering, Far/Mid-Infrared, and Raman Spectroscopies. *J. Phys. Chem. C* **2008**, *112*, 2193−2201.
(41) de Torresi, S. I. C.; Provazi, K.; Malta, M.; Torresi, R. M. Effect of Additives in the Stabilization of the Alpha Phase of $Ni(OH)_2$ Electrodes. *J. Electrochem. Soc.* **2001**, *148*, A1179−A1184.
(42) Vidotti, M.; Salvador, R. P.; de Torresi, S. I. C. Synthesis and Characterization of Stable Co and Cd Doped Nickel Hydroxide Nanoparticles for Electrochemical Applications. *Ultrason. Sonochem.* **2009**, *16*, 35−40.
(43) Hall, D. S.; Lockwood, D. J.; Poirier, S.; Bock, C.; MacDougall, B. R. Raman and Infrared Spectroscopy of α and β Phases of Thin Nickel Hydroxide Films Electrochemically Formed on Nickel. *J. Phys. Chem. A* **2012**, *116*, 6771−6784.
(44) Hall, D. S.; Lockwood, D. J.; Poirier, S.; Bock, C.; MacDougall, B. R. Applications of In Situ Raman Spectroscopy for Identifying Nickel Hydroxide Materials and Surface Layers during Chemical Aging. *ACS Appl. Mater. Interfaces* **2014**, *6*, 3141−3149.
(45) Kim, M. S.; Hwang, T. S.; Kim, K. B. A Study of the Electrochemical Redox Behavior of Electrochemically Precipitated Nickel Hydroxides Using Electrochemical Quartz Crystal Microbalance. *J. Electrochem. Soc.* **1997**, *144*, 1537−1543.
(46) MacArthur, D. M. The Hydrated Nickel Hydroxide Electrode Potential Sweep Experiments. *J. Electrochem. Soc.* **1970**, *117*, 422−426.
(47) Barnard, R.; Randell, C. F.; Tye, F. L. Studies Concerning Charged Nickel-Hydroxide Electrodes 0.1. Measurement of Reversible Potentials. *J. Appl. Electrochem.* **1980**, *10*, 109−125.
(48) de Faria, D. L. A.; Venâncio Silva, S.; de Oliveira, M. T. Raman Microspectroscopy of Some Iron Oxides and Oxyhydroxides. *J. Raman Spectrosc.* **1997**, *28*, 873−878.
(49) Lu, Z.; Wenwen, X.; Zhu, W.; Yang, Q.; Lei, X.; Liu, J.; Li, Y.; Sun, X.; Duan, X. Three-Dimensional NiFe Layered Double Hydroxide Film for High-Efficiency Oxygen Evolution Reaction. *Chem. Commun.* **2014**, *50*, 6479−6482.
(50) Santra, A. K.; Rao, C. N. R. Surface Alloy Formation in Pd/Ag, Cu/Au and Ni/Au Bimetallic Overlayers. *Appl. Surf. Sci.* **1995**, *84*, 347−350.
(51) Zafeiratos, S.; Kennou, S. Photoelectron Spectroscopy Study of Surface Alloying in the Au/Ni (S) 5(0 0 1) × (1 1 1) System. *Appl. Surf. Sci.* **2001**, *173*, 69−75.

DOI: 10.1021/acs.jpcc.5b00105
J. Phys. Chem. C 2015, 119, 7243−7254